

# Nonvolatile Electrochemical Random-Access Memory under Short Circuit

Diana S. Kim, Virgil J. Watkins, Laszlo A. Cline, Jingxian Li, Kai Sun, Joshua D. Sugar, Elliot J. Fuller, A. Alec Talin, and Yiyang Li\*

Electrochemical random-access memory (ECRAM) is a recently developed and highly promising analog resistive memory element for in-memory computing. One longstanding challenge of ECRAM is attaining retention time beyond a few hours. This short retention has precluded ECRAM from being considered for inference classification in deep neural networks, which is likely the largest opportunity for in-memory computing. In this work, an ECRAM cell with orders of magnitude longer retention than previously achieved is developed, and which is anticipated to exceed ten years at 85 °C. This study hypothesizes that the origin of this exceptional retention is phase separation, which enables the formation of multiple effectively equilibrium resistance states. This work highlights the promises and opportunities to use phase separation to yield ECRAM cells with exceptionally long, and potentially permanent, retention times.

## 1. Introduction

In-memory computing using analog resistive nonvolatile memory is highly attractive for data-heavy workflows like artificial intelligence.<sup>[1–4]</sup> By co-locating the memory and processing elements on a single device, in-memory analog computing is potentially much faster and more energy efficient than optimized digital computers.<sup>[1,5]</sup> A grand challenge has been to identify the best analog resistive memory element at the core of in-memory computing; proposed technologies include floating

gate memory,<sup>[6]</sup> phase-change memory (PCM),<sup>[7–9]</sup> ferroelectric transistors,<sup>[10,11]</sup> resistive redox memory (ReRAM),<sup>[12–17]</sup> and magnetic tunnel junction memory.<sup>[18]</sup> Unfortunately, none of these technologies have been able to meet all the demands of in-memory computing.

Electrochemical random-access memory, or ECRAM, is a promising recently developed device for analog in-memory computing.<sup>[19–46]</sup> ECRAM stores analog information states by electrochemically shuttling guest dopant ions like lithium ions, protons, or oxygen vacancies between two mixed-conducting host materials. Like ReRAM, ECRAM also stores and switches information through ion migration and the resulting


change in valence and electronic conductivity; however, unlike ReRAM, ECRAM contains a solid electrolyte, enabling accurate, linear, and deterministic changes in the resistance state. Since research in ECRAM has dramatically increased from 2017,<sup>[21,22]</sup> it has met many of the requirements for analog in-memory computing, including linear and symmetric among hundreds of analog states; low read and write currents, voltages, and energies; parallel weight updates;<sup>[23,35]</sup> CMOS-compatible materials with back-end-of-the-line (BEOL) thermal budgets;<sup>[27,28,47]</sup> and scaled sub-micrometer sized devices.<sup>[24,28]</sup> Recently, sub-microsecond switching times have been shown using protons-based ECRAM into polymers,<sup>[23,48]</sup> MXenes,<sup>[34]</sup> and tungsten oxides.<sup>[28]</sup> These developments make ECRAM highly promising for on-line training, which aims to identify the correct analog resistance states (or weights) of a network using the training set of pre-classified data. An even larger application of in-memory computing is inference, which uses a pretrained network to classify new data. Inference is not only simpler to conduct in analog, but is more ubiquitous because all distributed devices, including ones with very limited energy budgets, would use inference to classify new data.

An overarching challenge that has precluded ECRAM from inference accelerators is insufficient retention, generally only several hours at room temperature,<sup>[22,25–27]</sup> and much lower than the ten years at 85 °C benchmark for ReRAM, PCM, and floating gate memory. Moreover, nearly all retention studies utilize an electronic switch that keeps the gate and channel electrodes under “open circuit,” while this switch can provide several hours of retention in larger devices >10 μm, leakage currents in the switch will preclude retention times in scaled

D. S. Kim, V. J. Watkins, L. A. Cline, J. Li, K. Sun, Y. Li  
 Materials Science and Engineering  
 University of Michigan  
 Ann Arbor, MI 48109, USA  
 E-mail: yiyangli@umich.edu

D. S. Kim  
 Macromolecular Science and Engineering  
 University of Michigan  
 Ann Arbor, MI 48109, USA

J. D. Sugar, E. J. Fuller, A. A. Talin  
 Sandia National Laboratories  
 Livermore, CA 94550, USA

 The ORCID identification number(s) for the author(s) of this article can be found under <https://doi.org/10.1002/aelm.202200958>.

© 2022 The Authors. Advanced Electronic Materials published by Wiley-VCH GmbH. This is an open access article under the terms of the Creative Commons Attribution License, which permits use, distribution and reproduction in any medium, provided the original work is properly cited.

DOI: 10.1002/aelm.202200958

sub-micrometer devices.<sup>[25]</sup> A recent study using a 100-nm proton-based ECRAM shows only about 100 s retention time due to this scaling-retention challenge.<sup>[28]</sup> We have previously attempted to solve this problem by replacing highly mobile protons and lithium ions with the immobile oxygen ion,<sup>[25]</sup> effectively creating an “ionic switch” that can retain state under short circuit; however, this device would only retain state for about 1 d at 25 °C, and degrades rapidly to only  $\approx 100$  s at 70 °C under short circuit. Due to these challenges, it is believed that ECRAM will not be able to meet the needs of analog inference.

In this work, we demonstrate a nonvolatile ECRAM with a short-circuit retention time several orders of magnitude higher than previously shown in ECRAM, and can likely meet the ten years at 85 °C benchmark for binary states. By analyzing the electrochemical currents, we believe that this unprecedented retention time arises from phase separation into oxygen-rich and oxygen-poor phases of the amorphous tungsten oxide materials used in the ECRAM cell. This yields nonvolatile change in the ion concentration that does not fully reverse upon applying short circuit conditions after switching. Although additional material selection and device engineering are needed to realize the requirements necessary for an inference engine, our work shows that harnessing phase separation can provide a powerful means to enable nonvolatile ECRAM to attain the necessary retention times for analog inference.

## 2. Results and Discussion

### 2.1. Tungsten Suboxide ECRAM Devices

Our ECRAM cells consist of 50 nm of amorphous tungsten suboxide ( $\text{WO}_{3-x}$ ) deposited on opposite sides of a single-crystal yttria-stabilized zirconia (YSZ) substrate using reactive sputtering (Figure 1a). Figure S1 (Supporting Information) uses the X-ray diffraction pattern to confirm the  $\text{WO}_{3-x}$  material is amorphous. Three Pt current collectors are sputtering over shadow

masks (Figure S2, Supporting Information). While tungsten oxide can intercalate several ions, YSZ is a well-researched oxygen conductor<sup>[49]</sup> used for solid oxide fuel cells and, more recently, applied for ECRAM analog memory devices.<sup>[25,31,32]</sup> Finally, a passivation layer of  $\text{HfO}_x$  is deposited to reduce the oxidation of  $\text{WO}_{3-x}$  with the environment. Except for the YSZ, all processes are back-end of the line (BEOL) compatible, with deposition temperatures below 200 °C. Energy-dispersive spectroscopy (Figure S3, Supporting Information) of this suboxide suggests a metal-to-oxygen ratio of 2:5, yielding  $\text{WO}_{3-x}$  where  $X \approx 0.5$ . We operate this device by applying a positive gate voltage ( $V_G$ , Figure 1a) to potentiate and a negative gate voltage to depress; during retention, we ground the gate by applying 0 V, short-circuiting it to the channel. More details on the operating principles of ECRAM are given in Note S1 (Supporting Information). Because we do not use a selector or a switch with nonzero electronic leakage current in series with the gate, as done in most past research, our ability to retain state under short circuit can be scaled to smaller devices.<sup>[25]</sup>

Like other ECRAM cells, this device possesses linear and symmetric analog switching, with at least 200 distinct analog states (Figure 1b). This 3 $\times$  conductance modulation is generally consistent with other ECRAM work, and is close to the 10 $\times$  target for in-memory computing.<sup>[50]</sup> The write current density of  $10^{-14}$  A  $\mu\text{m}^{-2}$  is comparable with other ECRAM cells,<sup>[25]</sup> and much lower than that of phase-change, ReRAM, and floating gate memory. The channel conductance, at  $\approx 100$   $\mu\text{S}$ , is generally higher than optimal for in-memory computing.<sup>[50]</sup> However, the channel conductance drops by about an order of magnitude between 200 and 40 °C (Figure 1c). Because the electron concentration is controlled by the oxygen vacancy doping level and controlled using electrochemistry, the temperature dependence likely results from the positive temperature coefficient of electron mobility commonly seen in polaron conductors like  $\text{WO}_3$ .<sup>[51]</sup> As a result, while the conductance state should be set at high temperatures, inference could be conducted at near-room temperatures with much lower electronic conductances and

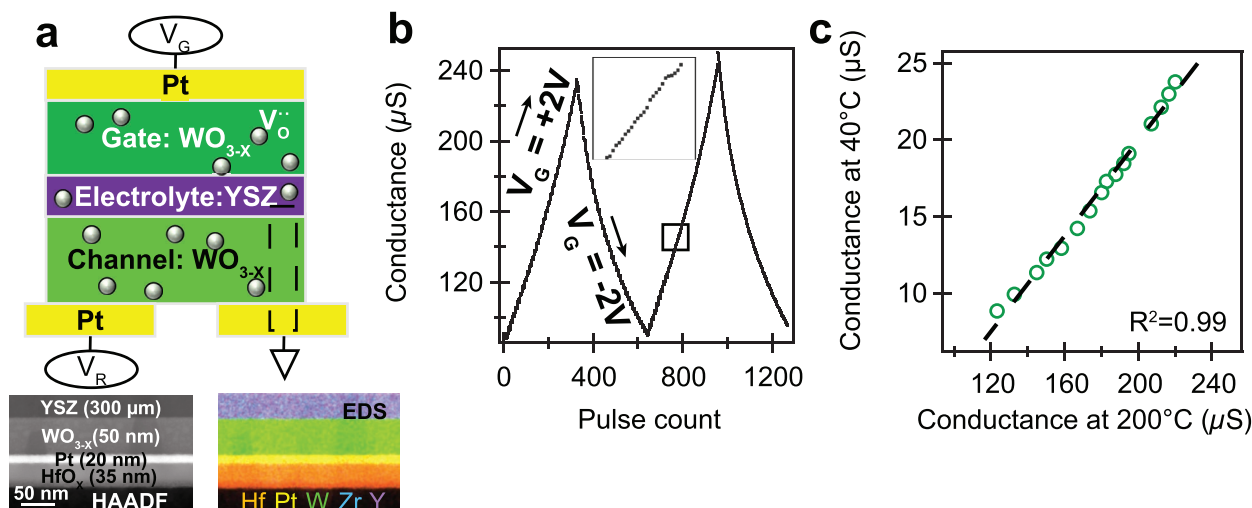


**Figure 1.** Tungsten suboxide based ECRAM cell used in this work. a) Schematic and cross-section TEM of the  $\text{WO}_{3-x}$  ECRAM cell. This cell stores and switches analog information states as the concentration of oxygen vacancy ions in the channel. b) Linear and symmetric switching among many analog states. Each pulse applies a voltage of  $\pm 2$  V for 30 s. c) There exists a direct linear mapping of the conductance at 200 °C and the conductance at 40 °C.

consequently improved power efficiencies. Further decrease of the conductance by at least one order of magnitude can be achieved by simply reducing the width-to-length ratio from 16:1 to 1:1, and would place this cell well within the target of  $\approx 1$  M $\Omega$  for analog inference. The switching time and temperature can be decreased by reducing the YSZ thickness from  $\approx 300$   $\mu\text{m}$  to  $<1000$  nm, as has been shown in our past work.<sup>[25]</sup>

## 2.2. Demonstration of Nonvolatile ECRAM

Having shown that we can switch to any resistance state within the range by applying a gate voltage for a given amount of time (Figure 1b), we next investigate the retention behavior under short-circuit. In Figure 2a, we monitor the channel conductance when  $V_G = 0$  V after the device is set to different resistance states. To our surprise, after a volatile transient response, the conductance states ultimately settle at different values, and not to an equilibrium value as shown in other ECRAM.<sup>[25,52]</sup> A tangent line extrapolation over the last 300 s confirms that the channel conductances are not converging. While we only show five analog states due to experimental time constraints, we anticipate that each switched state in Figure 1b yields a distinct retention profile and a different final conductance. Whereas applying a gate voltage of 0 V without a switch to other ECRAM erases the previously programming resistance state (Figure S4, Supporting Information), this ECRAM cell shows that a non-volatile change in resistance can be achieved even under short circuit at elevated temperatures.

In Figure 2b, we monitor nonvolatility over 24 h at 200 °C from the high resistance and the low resistance state with  $V_G = 0$  V. Once again, we observe a volatile transient response and a nonvolatile response. Interestingly, while the conductance of the high-resistance state is very stable, there is a slight decrease in the conductance of the low-resistance state over time. We hypothesize this is a result of slow atmospheric oxidation

of the suboxides, despite the  $\text{HfO}_2$  protection layer. However, even a tangent line extrapolation suggests that the high- and low-resistance states will not converge until at least 150 h at 200 °C. We note that the slopes of these tangent lines decrease over time and approach 0. If the slope reaches 0, the conductance values will not converge, and the projected retention approaches infinity. In the absence of atmospheric oxidation, we anticipate that the tangent line slope will eventually reach 0, and that the cell will exhibit a permanent change in the channel conductance. However, further work will be necessary to confirm the ultimate retention times, especially given the convoluting effects of oxidation.

We compare the retention time of our  $\text{WO}_x$ -ECRAM with that of other ECRAM cells and with two-terminal filamentary ReRAM based on  $\text{HfO}_x$  (Figure 2c). Our retention times are about 3–4 orders of magnitude higher than our previous anatase  $\text{TiO}_2$ -based ECRAM cells using a similar single-crystal YSZ electrolyte substrate.<sup>[25]</sup> More excitingly, both our achieved retention time of 24 h and tangent-line extrapolated result of  $>150$  h at 200 °C are comparable to that of  $\text{HfO}_x$ -based two-terminal ReRAM devices at the same temperature. It is well accepted that these ReRAM devices yield ten years of retention time at 85 °C.<sup>[53–56]</sup>

We next aim to project the retention time to lower temperatures. In our device, the low- and high-resistance states do not converge in 24 h at 200 °C, and may never converge. Thus, it is not possible to directly extrapolate the retention time by measuring when the high- and low-resistance states converge at different temperatures. Instead, we treat the gate electrochemical current  $I_G$  as proportional to the ionic conductivity of the YSZ electrolyte, as shown in previous work;<sup>[25]</sup> in Figure S5 (Supporting Information), we confirm that this gate current  $I$  has an Arrhenius relationship with an activation energy equal to 1.2 eV. As we will show in the next section, the channel conductance is controlled by the integral of the gate current  $I_G$ , or the gate charge  $Q$ . As a result, if the ionic conductivity

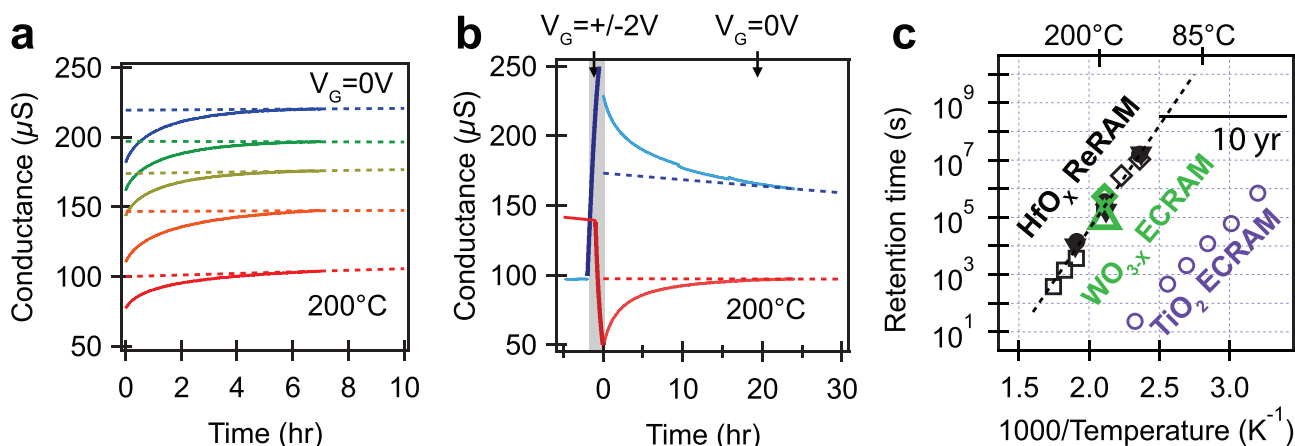


**Figure 2.** ECRAM retention characteristics when the gate and channel are shorted. a) After setting to a given state, our ECRAM cells will stabilize into one of several different analog resistance states. Dashed lines are tangent line constructions that project different conductance values as a function of time. b) Retention times held for 24 h from the low-resistance (blue) and high-resistance (red) states.  $t = 0$  h signify when retention measurements start, which occur after a 1 or 2 h switching at  $V_G = \pm 2$  V. The tangents lines to these retention profiles converge after about 150 h at 200 °C. c) Comparison of retention times of  $\text{WO}_{3-x}$  ECRAM with filament-based ReRAM<sup>[53–56]</sup> and past  $\text{TiO}_2$ -based ECRAM.<sup>[25]</sup> Each different marker shape for  $\text{HfO}_x$  ReRAM indicates results from a different paper. The two  $\text{WO}_{3-x}$ -ECRAM retention times at 24 (triangle) and 150 (diamond) h equals the time for the experiment in (b) and the extrapolated tangent line convergence. Both values likely underestimate the retention time.

and resulting gate current decreases by a factor of 10, then we expect it will take ten times longer to yield a certain gate charge  $Q$ , and the retention time will be ten times higher. Because the ionic resistivity of YSZ has an activation energy of 1.1–1.2 eV (Figure S5, Supporting Information), we expect that the gate current at 85 °C will be about 6000–13 000 times lower than that at 200 °C. This yields an expected retention time from 24 h at 200 °C to 15–35 years at 85 °C. We note that this is expected to be a lower bound, as this only represents an extrapolation for our 24-h experiment at 200 °C.

### 2.3. Investigation of Electrochemical Currents

To better understand the mechanism for nonvolatile ECRAM, we monitor the gate electrochemical current during the switching and retention process. In ECRAM cells containing an electrolyte that conducts ions but blocks electrons, the ionic current through the electrolyte must equal the electronic current passed between gate and channel (via the external programming circuit)  $I_G$  due to charge balance. This electrochemical current  $I_G$  is proportional to the time derivative of

$X_1$  ( $I_G \sim \frac{dX_1}{dt}$ ), defined as the concentration of oxygen vacancy ions in the channel. Similarly, the electrochemical charge  $Q$  ( $Q(t) = \int I_G(t) dt$ ) describes the net change in the concentration of ions ( $\Delta X_1$ ) in the channel over time.

In Figure 3a, we monitor the gate current  $I_G$  and charge  $Q$  during a 1 h depression (–2 V) followed by a 24 h retention (0 V), during the same experiment as in Figure 2b. During depression,  $I_G < 0$  implies that oxygen vacancies move out of the channel, decreasing the channel conductance (Figure 2b). Based on a  $\text{WO}_{3-x}$  film thickness of 50 nm, a planar area of 8 mm<sup>2</sup>, a density of 7 g cm<sup>–3</sup>, and –400  $\mu\text{C}$  of charge transferred (Figure 3a), we estimate the change in oxygen vacancy concentration to be about  $4 \times 10^{20}$  cm<sup>–3</sup>. This is  $\approx 1\%$  increase

in the oxygen atoms and  $\approx 5\%$  decrease in the oxygen vacancy concentration from the initial  $\text{WO}_{2.5}$  film (Figure S3, Supporting Information). However, upon applying 0 V, the electrochemical current  $I_G$  reverses ( $I_G > 0$ ), suggesting that the oxygen vacancies now enter the channel, and are responsible for the transient increase in the channel conductance (Figure 2b). This electrochemical current rapidly decreases and approaches 0. However, even after 24 h,  $Q$  does not revert to 0. Since  $(Q \sim \Delta X_1) < 0$ , the oxygen vacancy concentration at the end of the 24 h is lower than the oxygen vacancy concentration before the depression, a result consistent with the nonvolatile decrease in the channel conductance  $G$  (Figure 2b). Furthermore, the electrochemical current  $I_G$  has fallen to such a low value that it is unlikely that  $Q$  will reach 0. This strongly suggests that the cell has reached a new, permanent change in the ion concentration ( $X_1$ ), just as it reached a different value for  $G$  in Figure 2b.

In Figure 3b, we show the same behavior during a 2 h potentiation at  $V_G = +2$  V followed by a 24 h retention at 0 V, taken immediately after the result in Figure 3b. The channel conductance during the measurement was plotted in Figure 2b. We start  $Q$  at –140  $\mu\text{C}$ , continuing from the end of the 0 V retention in Figure 3a. In this case, +2 V yields a positive current while the following 0 V retention yields a negative current. As in the case for the depression in Figure 3b, the total integrated charge  $Q$  during retention is much lower than that of the potentiation, even as the current is essentially 0. This result is again consistent with nonvolatility observed in Figure 2b after potentiation. In Figure 3c, we confirm that the conductance of the channel  $G$  is effectively only a function of the integrated gate electrochemical charge  $Q$ , and nearly independent of other variables. Therefore, changes in the charge  $Q$  are directly linked to changes in the conductance  $G$ .

Summarizing our results in this section, we analyze the electrochemical current on the gate to show that holding the cell at 0 V for 24 h fails to recover the  $Q$  that was applied during the

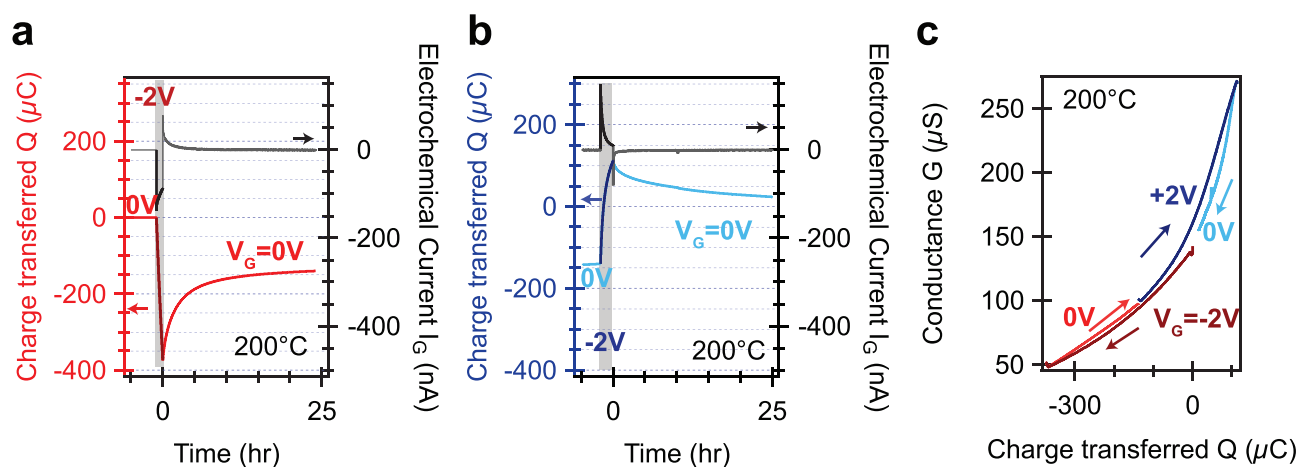


**Figure 3.** The gate electrochemical charge ( $Q$ ) and currents ( $I_G$ ) during switching and retention. a) The gate current is negative when –2 V is applied, and rebounds during retention. However, the net charge transferred  $Q$  converges to –140  $\mu\text{C}$  even after 24 h, suggesting a nonvolatile change in the ion concentration of the channel. b) A +2 V potentiation is applied after the measurements in (a). Once again, the net charge transferred after 24 h once again appears to converge to a different value, suggesting a nonvolatile change in the channel ion concentration despite the 24 h retention measurement at short circuit. c) The electrochemical charge transferred  $Q$  directly maps to the channel conductance  $G$ , consistent with why both these values are nonvolatile.

previous potentiation and depression. This provides additional evidence that the change in the channel conductance shown in Figure 2 results from a nonvolatile change in the oxygen vacancy concentration  $X_1$  of the channel.

#### 2.4. Phase Separation as One Possible Origin of Nonvolatility in ECRAM

Having shown a nonvolatile change in the channel conductance  $G$  and the ion concentration  $X_1$  under short-circuit, we seek to understand how this nonvolatile ECRAM differs from previously demonstrated ECRAM, which are all volatile in comparison. Most volatile ECRAM requires an electronic switch to show any retention beyond a few seconds. In this section, we propose one possible mechanism for how the nonvolatile ECRAM in this work differ from past volatile ECRAM. In Figure 4a,b, we schematically illustrate ECRAM cells in two states. Figure 4a shows a state where the channel ion concentration  $X_1$  equals the gate ion concentration  $X_2$ . Figure 4b shows a state where  $X_1 \neq X_2$ . The underlying mechanism for all ECRAM devices is that, by applying an electrochemical voltage pulse, we

can switch the cell from state 1 to state 2, as well as to a number of other analog resistance states.

##### 2.4.1. Volatile ECRAM Based on Solid Solution

In previously demonstrated types of ECRAM, it is believed that there is only one equilibrium state. This usually occurs when  $X_1 = X_2$  (Figure 4a). When the gate and channel are shorted, the ECRAM cell will revert to this equilibrium state. We propose that ECRAM cells that require a switch should be considered volatile ECRAM because, under equilibrium, they will all revert back to a single resistance state in Figure 4a. One way to rationalize the relaxation of state 2 to state 1 under short circuit is to consider this a diffusion dominated process where ions migrate from high to low concentrations. Equilibrium is only achieved when  $X_1 = X_2$ , yielding a single equilibrium analog state, and is consistent with drift-diffusion modeling.<sup>[43]</sup>

A more generalizable framework is to recognize that the mass flux follows the spatial gradient of the ion's chemical potential  $\mu$ , rather than the gradient of the ion concentration  $X$ . Equilibrium is attained when the ion chemical potential in the channel  $\mu(X_1)$  equals that of the gate  $\mu(X_2)$ . When the chemical potential  $\mu(X)$  increases monotonically with  $X$  (Figure 4c), which is the case for when the ion forms a solid solution with the host, this equilibrium condition  $\mu(X_1) = \mu(X_2)$  is only attained when  $X_1 = X_2$ . This results in volatile ECRAM with only a single equilibrium state. We note that the exact shape of  $\mu(X)$  does not necessarily need to equal that Figure 4c; rather, it only needs to monotonically increase (or decrease) with the ion concentration  $X$ . For example, organic ECRAM operate like electrochemical capacitors<sup>[57]</sup> where  $Q = CV$ , but the monotonic relationship between voltage and charge would result in volatile behavior.

##### 2.4.2. Nonvolatile ECRAM Based on Phase Separation

As discussed in the previous paragraph, the thermodynamic equilibrium condition is that  $\mu(X_1) = \mu(X_2)$ . If this condition can be achieved when  $X_1 \neq X_2$ , such as through the chemical potential profile shown in Figure 4d, then the switched state B (Figure 4b) is also in equilibrium and will not revert to state A. In fact, there is likely a very large, possibly continuous, number of analog equilibrium or near-equilibrium states (see caption in Figure 4d for details). The flat chemical potential profile shown in Figure 4d is commonly seen in phase-separating materials systems, where the common tangent construction of the Gibbs free energy yield phase separation (Figure S6, Supporting Information). Such phase-separating systems cannot be modeled using drift-diffusion type equations<sup>[39]</sup> because ions do not necessarily move from high to low concentrations.<sup>[58,59]</sup> While phase separation is difficult to probe in amorphous materials like our  $\text{WO}_{3-x}$  channel, our result nonetheless suggests that phase separation is a strong candidate for the origin of nonvolatility (Figures 3 and 4). It is well documented in other electrochemical systems like Li-ion batteries that phase separation is responsible for the simultaneous coexistence of ion-rich and ion-poor regions;<sup>[60–62]</sup> similarly, in nonvolatile ECRAM, phase separation can yield a

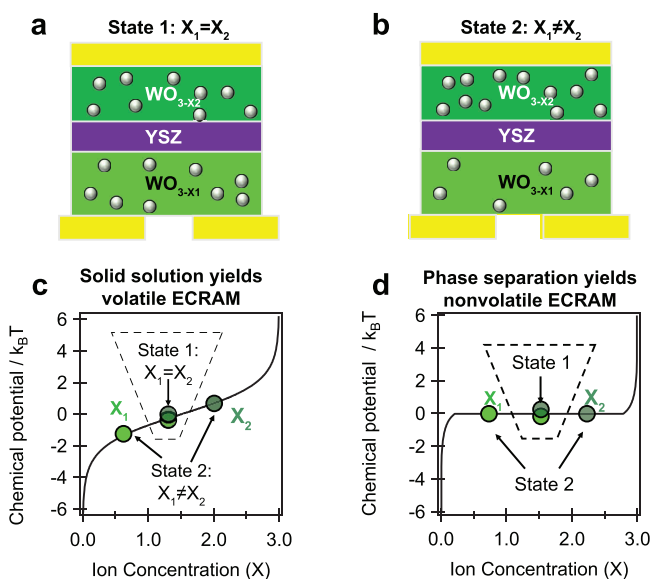


**Figure 4.** Phase separation as a proposed mechanism for the nonvolatile changes in channel ion concentration and electronic conductance. a,b) Two states of the ECRAM cell are schematically illustrated.  $X_1$  and  $X_2$  represent the concentration of ions in the channel and gate, respectively. a) State 1 occurs when  $X_1 = X_2$  and represents the initial state of the cell that uses the same material for the gate and the channel. b) State 2 is the general case where  $X_1 \neq X_2$ , and arises after switching. c) If the guest ion chemical potential increases monotonically with the ion concentration, then only state 1 is in equilibrium, and state 2 will eventually revert to state 1 over time. This yields volatile ECRAM. d) If there exists a plateau in the chemical potential, then both state 1 and 2 are stable, implying a nonvolatile change in  $X_2$ . This nonvolatility arises when the channel material separates into two or more phases. We note that, from a thermodynamic perspective, there ultimately is only one equilibrium configuration even in two-phase systems due to interfacial energy; however, the driving force to equilibrate interfaces is very small and will take much longer to equilibrate interfaces than to equilibrate compositional differences in a solid solution.

gate and a channel with different ion concentrations ( $X_1 \neq X_2$ ) that will not revert to  $X_1 = X_2$ . We note that, while phase separation typically describes the coexistence of two crystal structures, we did not observe any crystalline diffraction peaks (Figure S1, Supporting Information). As a result, we hypothesize this phase separation to occur between two amorphous states with different metal-to-oxygen ratios that coexist in equilibrium. Recent computational work suggests that there exists amorphous phase separation in tantalum oxide, a different refractory metal oxide.<sup>[63]</sup> Because amorphous materials are not sensitive to diffraction, future work using more advanced characterization techniques will be needed to verify phase separation.

Within this framework, we revisit our experimental results that show both a transient volatile response and a nonvolatile response. In Figures 2b and 3b, the channel conductance  $G$  and the gate charge  $Q$  decrease during depression but increases during the 24 h retention. However, this transient increase ( $\Delta Q = +200 \mu\text{C}$ ) is substantially less than the original decrease ( $\Delta Q = -380 \mu\text{C}$ ), and both  $Q$  and  $G$  ultimately settle to a state different from the initial  $Q$  and  $G$ . This is consistent with state 2 in that Figure 4b represents a different resistance than state 1 in Figure 4a; however, in this case, both states are considered equilibrium configurations. We believe that the steady-state, nonvolatile response is a result of phase separation, as  $\mu(X_1) = \mu(X_2)$ , both at the start and at the end of the measurement. The origin of the long transient response is not clear; some possibilities include the volatile response of an electrochemical double layer or the nucleation time for phase separation.

Finally, we note that our description in Figure 4d does not take into account the requirement to minimize interfaces in spinodal decomposition.<sup>[58,64]</sup> In this respect, there may only be one final, ultimate equilibrium configuration. However, to reach this final state, which may not be state 1 ( $X_1 = X_2$ ), it will take much longer than the timescales based on Fickian diffusion, and may not be reachable in experimental timescales. This process may be analogous to coarsening, which slows over time.<sup>[65]</sup> It is also unclear how this “coarsening” process will affect the measured electronic resistance, making it very difficult to understand the dynamics of reaching this final equilibrium state.

### 3. Discussion

Nonvolatile behavior and potentially permanent changes in channel conductance are paradigm changing for ECRAM and nonvolatile memory, especially considering the poor retention of previous reports at scale. The possibility of an ECRAM cell with multiple nonvolatile resistance states under short circuit is compelling for robust inference engines that operate throughout the lifetime of a product. The retention of such cells is orders of magnitude higher than past ECRAM research, and is comparable to that of HfO<sub>x</sub>-based ReRAM at 200 °C (Figure 2c). Our long retention times show that applications for ECRAM extend beyond on-line training, as suggested in past works.<sup>[23,28,35]</sup> Inference is not only more broadly applicable, but also one where requirements like switching time, temperature, and endurance are less stringent than for on-line training.

While the nonvolatile WO<sub>x</sub>-ECRAM is highly promising, there are several materials challenges that must be resolved.

The first need is to replace a single-crystal YSZ electrolyte used in this work with a thin-film electrolyte that can be sputter deposited on Si. We have included preliminary results of a WO<sub>3-x</sub>/YSZ/WO<sub>3-x</sub> ECRAM cell with a thin-film electrolyte with evidence of nonvolatile state retention which is the subject of future work (Figure S7, Supporting Information); however, additional work is required to achieve high reliability and reproducibility of this device. Creating a thin-film device is more practical for CMOS integration, and also substantially reduces the switching and settling times. Because the changes in the conductance states can be permanent due to phase separation (Figure 4d), we anticipate thin-film devices will also have excellent state retention, even if the ionic currents are higher due to thinner electrolytes. Other tasks include identifying new phase-separating materials with faster switching and shorter settling times. One such material is the well-studied SrCoO<sub>2.5</sub>, which undergoes a phase transition from the Brownmillerite SrCoO<sub>2.5</sub> to the perovskite SrCoO<sub>3</sub> phase.<sup>[66]</sup> We anticipate that further developments along these fronts may yield permanently nonvolatile ECRAM that can meet all requirements for analog inference.

### 4. Conclusions

In this work, we develop nonvolatile ECRAM using WO<sub>3-x</sub> where the change in the ion concentration and resistance change in the channel is permanent under short circuit. This likely results from phase separation, whereby the chemical potential of oxygen in the gate and channel are equal, even though their concentrations differ. Our results demonstrate several orders of magnitude increase in the retention time compared to past work, and matches that of state-of-the-art filament-based resistive memory technologies. This work opens a new paradigm for nonvolatile ECRAM, as well as highlights a design principle for identifying nonvolatile ECRAM materials.

### 5. Experimental Section

*Fabrication of WO<sub>3-x</sub> ECRAM Cells:* 300- $\mu\text{m}$ -thick, 1 cm square, single-crystal yttrium-stabilized zirconia (8 mol% Y<sub>2</sub>O<sub>3</sub> in ZrO<sub>2</sub>) substrates were purchased from MTIXTL and were used without further cleaning or treatment. 50 nm of WO<sub>3-x</sub> were sputtered on the gate side through an 8 mm square shadow mask using an AJA Orion-8 sputter system. The target was a 3-in. W target (99.95% purity) from Plasmaterials (Livermore, CA). The target power was 100 W. To make the suboxide, the sputter gas was a mixture of Ar:O<sub>2</sub> at a ratio of 85:15, controlled by mass flow controllers. The sputter gas pressure was 3 mtorr. The substrate to target distance was about 15 cm.

The 18-nm-thick gate Pt current collector was sputtered on top of the WO<sub>3-x</sub> layer using the same shadow mask without breaking vacuum. The target was a 2-in. Pt target; the sputter gas was 3 mtorr of pure argon. After depositing both the suboxide and metal layers, the substrate was flipped and the same WO<sub>3-x</sub> was deposited on the channel side with the same shadow mask. Finally, the two Pt current collectors were deposited on the channel with a different shadow mask (Figure S2, Supporting Information). This mask has two square regions separated by 0.5 mm. All shadow masks were made from a 0.13 mm thick stainless steel sheet, and cut using a CO<sub>2</sub> laser by Stencils Unlimited (Tualatin, OR). All sputtering was done at room temperature; no additional annealing was conducted.

Finally, to protect the cell from environmental oxidation, atomic layer deposition was used to deposit 35 nm of HfO<sub>x</sub> on the channel side of the ECRAM device. The HfO<sub>x</sub> layer was deposited using a Veeco Fiji ALD plasma/thermal assisted atomic layer deposition at the Lurie Nanofabrication Facility. A thermal deposition was done at 200 °C, using the precursor TDMAH and Argon gas, and ran for 297 cycles, at a rate of ≈1 Å cycle<sup>-1</sup> and 24 s cycle<sup>-1</sup>. The film thickness was measured to be ≈35 nm (Figure 1a). While the HfO<sub>x</sub> passivation layer reduced environmental oxidation, it did not fully eliminate oxidation at these elevated temperatures, as seen in the long retention measurements (Figure 2).

**Device Measurements:** After fabrication, the cell was placed in a custom-built, six-probe Nextron MPS-Ceramic Heater CHH750, environmentally controlled probe station. The two electrodes on the channel directly contacted the Rh probes. The gate current collector rested on a Si substrate with 50 nm of Pt sputtered, and the Rh probe contacts the Pt. The environment was further controlled by flowing 5N ultra high-purity Ar at a flow rate of 87 standard cubic centimeters per minute (sccm) controlled by an Omega mass flow controller. A Swagelok check valve was placed to pressurize the chamber to ≈50 torr (1 pound per square inch) above ambient, which prevents backflow of air into the chamber. A portable Zirox ZR5 oxygen sensor showed that the oxygen concentration in the Ar flow gas is about 3 parts per million, and likely caused the oxidation shown in Figure 2. It was noted that flowing Ar was much more effectively at forming a thermal contact between the heater and the chip, compared to pulling a vacuum.

Device measurements were conducted using a Bio-logic SP300 bipotentiostat. Channel was used to apply the gate voltage, while channel 2 was used to measure the channel conductance. The channel conductance was measured by alternating between +10 and -10 mV for 30 or 60 s each, then taking the average absolute current averaged over 60 or 120 s.

**TEM Measurements:** STEM measurements at the University of Michigan were taken using a Thermo Fisher Talos F200X G2, a 200 kV FEG scanning transmission electron microscope operated in STEM mode. The Velox software was used for STEM images and EDS data acquisitions. The TEM specimen was prepared using a Thermo-Fisher Helios 650 Xe Plasma FIB. The final beam condition was set at 12 keV 10 pA for the liftoff polishing.

TEM sample preparation at Sandia National Labs was performed with a ThermoFisher Helios Nanolab 660 Dualbeam instrument. The sample was extracted and thinned with 30 kV Ga<sup>+</sup> ions and then final-polished at 5 kV. SNL STEM analysis was performed with a monochromated, aberration corrected ThermoFisher Titan Themis Z operated at 300 kV with a SuperX EDS detector and Gatan Quantum 969 GIF.

## Supporting Information

Supporting Information is available from the Wiley Online Library or from the author.

## Acknowledgements

This work at the University of Michigan was supported by the National Science Foundation under Grant No. ECCS-2106225, startup funding from the University of Michigan College of Engineering, and subcontracts from Sandia National Laboratories under the Diversity Initiative and Campus Executive Programs. The work at Sandia National Labs was supported by the Laboratory-Directed Research and Development (LDRD) program. Sandia National Laboratories is a multi-mission laboratory managed and operated by National Technology and Engineering Solutions of Sandia, LLC, a wholly owned subsidiary of Honeywell International Inc., for the U.S. Department of Energy's National Nuclear Security Administration under Contract No. DE-NA-0003525. A.A.T. was partly supported by the DOE Office of Science Research Program for Microelectronics Codesign (sponsored

by ASCR, BES, HEP, NP, and FES) through the Abisko Project, PM Robinson Pino (ASCR). This paper describes objective technical results and analysis. Any subjective views or opinions that might be expressed in the paper do not necessarily represent the views of the U.S. Department of Energy or the United States Government. The authors acknowledge the University of Michigan College of Engineering for financial support and the Michigan Center for Materials Characterization for use of the instruments and staff assistance. Part of this work was conducted in part of the University of Michigan Lurie Nanofabrication Facility.

## Conflict of Interest

The authors declare no conflict of interest.

## Author Contributions

D.S.K., V.J.W., L.A.C. and J.L. fabricated the devices and conducted the measurements. K.S. and J.D.S. conducted TEM measurements. All authors contributed to writing and revising the manuscript.

## Data Availability Statement

The data that support the findings of this study are openly available in Materials Commons at <https://doi.org/10.13011/m3-tz6h-ht18>, Inquires about how to access and use this dataset can be directed to the corresponding author.

## Keywords

in-memory computing, oxygen vacancies, retention, tungsten oxide

Received: August 22, 2022

Revised: October 4, 2022

Published online: November 15, 2022

- [1] A. Mehonic, A. J. Kenyon, *Nature* **2022**, 604, 255.
- [2] D. Ielmini, H.-S. P. Wong, *Nat. Electron.* **2018**, 1, 333.
- [3] Q. Xia, J. J. Yang, *Nat. Mater.* **2019**, 18, 309.
- [4] W. Wan, R. Kubendran, C. Schaefer, S. B. Eryilmaz, W. Zhang, D. Wu, S. Deiss, P. Raina, H. Qian, B. Gao, S. Joshi, H. Wu, H.-S. P. Wong, G. Cauwenberghs, *Nature* **2022**, 608, 504.
- [5] M. J. Marinella, S. Agarwal, A. Hsia, I. Richter, R. Jacobs-Gedrim, J. Niroula, S. J. Plimpton, E. Ipek, C. D. James, *IEEE J. Emerging Sel. Top. Circuits Syst.* **2018**, 8, 86.
- [6] J. Hasler, *Proc. IEEE* **2020**, 108, 1283.
- [7] S. Ambrogio, P. Narayanan, H. Tsai, C. Mackin, K. Spoon, A. Chen, A. Fasoli, A. Friz, G. W. Burr, in *2020 Int. Symp. VLSI Technology, Systems and Applications (VLSI-TSA)*, IEEE, Genova, Italy **2020**, pp. 119–120.
- [8] S. Ambrogio, P. Narayanan, H. Tsai, R. M. Shelby, I. Boybat, C. di Nolfo, S. Sidler, M. Giordano, M. Bodini, N. C. P. Farinha, B. Killeen, C. Cheng, Y. Jaoudi, G. W. Burr, *Nature* **2018**, 558, 60.
- [9] C. Mackin, M. J. Rasch, A. Chen, J. Timcheck, R. L. Bruce, N. Li, P. Narayanan, S. Ambrogio, M. Le Gallo, S. R. Nandakumar, A. Fasoli, J. Luquin, A. Friz, A. Sebastian, H. Tsai, G. W. Burr, *Nat. Commun.* **2022**, 13, 3765.
- [10] A. I. Khan, A. Keshavarzi, S. Datta, *Nat. Electron.* **2020**, 3, 588.
- [11] P. Wang, S. Yu, *MRS Commun.* **2020**, 10, 538.

- [12] Z. Wang, H. Wu, G. W. Burr, C. S. Hwang, K. L. Wang, Q. Xia, J. J. Yang, *Nat. Rev. Mater.* **2020**, 5, 173.
- [13] P. Yao, H. Wu, B. Gao, J. Tang, Q. Zhang, W. Zhang, J. J. Yang, H. Qian, *Nature* **2020**, 577, 641.
- [14] M. Hu, C. E. Graves, C. Li, Y. Li, N. Ge, E. Montgomery, N. Davila, H. Jiang, R. S. Williams, J. J. Yang, Q. Xia, J. P. Strachan, *Adv. Mater.* **2018**, 30, 1705914.
- [15] T. Stecconi, R. Guido, L. Berchiolla, A. La Porta, J. Weiss, Y. Popoff, M. Halter, M. Sousa, F. Horst, D. Dávila, U. Drechsler, R. Dittmann, B. J. Offrein, V. Bragaglia, *Adv. Electron. Mater.* **2022**, 8, 2200448.
- [16] R. Dittmann, S. Menzel, R. Waser, *Adv. Phys.* **2022**, 70, 155.
- [17] R. Waser, R. Dittmann, G. Staikov, K. Szot, *Adv. Mater.* **2009**, 21, 2632.
- [18] S. Liu, T. P. Xiao, C. Cui, J. A. C. Incorvia, C. H. Bennett, M. J. Marinella, *Appl. Phys. Lett.* **2021**, 118, 202405.
- [19] J. Shi, S. D. Ha, Y. Zhou, F. Schoofs, S. Ramanathan, *Nat. Commun.* **2013**, 4, 2676.
- [20] J. D. Greenlee, C. F. Petersburg, W. G. Daly, F. M. Alamgir, W. Alan Doolittle, *Appl. Phys. Lett.* **2013**, 102, 213502.
- [21] E. J. Fuller, F. E. Gabaly, F. Léonard, S. Agarwal, S. J. Plimpton, R. B. Jacobs-Gedrim, C. D. James, M. J. Marinella, A. A. Talin, *Adv. Mater.* **2017**, 29, 1604310.
- [22] Y. van de Burgt, E. Lubberman, E. J. Fuller, S. T. Keene, G. C. Faria, S. Agarwal, M. J. Marinella, A. A. Talin, A. Salleo, *Nat. Mater.* **2017**, 16, 414.
- [23] E. J. Fuller, S. T. Keene, A. Melianas, Z. Wang, S. Agarwal, Y. Li, Y. Tuchman, C. D. James, M. J. Marinella, J. J. Yang, A. Salleo, A. A. Talin, *Science* **2019**, 364, 570.
- [24] J. Tang, D. Bishop, S. Kim, M. Copel, T. Gokmen, T. Todorov, S. Shin, K.-T. Lee, P. Solomon, K. Chan, W. Haensch, J. Rozen, in *2018 IEEE Int. Electron Devices Meeting (IEDM)*, IEEE, San Francisco, USA **2018**, pp. 13.1.1–13.1.4.
- [25] Y. Li, E. J. Fuller, J. D. Sugar, S. Yoo, D. S. Ashby, C. H. Bennett, R. D. Horton, M. S. Bartsch, M. J. Marinella, W. D. Lu, A. A. Talin, *Adv. Mater.* **2020**, 32, 2003984.
- [26] Y. Li, E. J. Fuller, S. Asapu, S. Agarwal, T. Kurita, J. J. Yang, A. A. Talin, *ACS Appl. Mater. Interfaces* **2019**, 11, 38982.
- [27] S. Kim, T. Todorov, M. Onen, T. Gokmen, D. Bishop, P. Solomon, K.-T. Lee, M. Copel, D. B. Farmer, J. A. Ott, T. Ando, H. Miyazoe, V. Narayanan, J. Rozen, in *2019 IEEE Int. Electron Devices Meeting (IEDM)*, IEEE, San Francisco, USA **2019**, pp. 35.7.1–35.7.4.
- [28] M. Onen, N. Emond, B. Wang, D. Zhang, F. M. Ross, J. Li, B. Yildiz, J. A. Del Alamo, *Science* **2022**, 377, 539.
- [29] X. Yao, K. Klyukin, W. Lu, M. Onen, S. Ryu, D. Kim, N. Emond, I. Waluyo, A. Hunt, J. A. del Alamo, J. Li, B. Yildiz, *Nat. Commun.* **2020**, 11, 3134.
- [30] J. Lee, R. D. Nikam, M. Kwak, H. Hwang, *ACS Appl. Mater. Interfaces* **2022**, 14, 13450.
- [31] J. Lee, R. D. Nikam, M. Kwak, H. Kwak, S. Kim, H. Hwang, *Adv. Electron. Mater.* **2021**, 7, 2100219.
- [32] R. D. Nikam, M. Kwak, H. Hwang, *Adv. Electron. Mater.* **2021**, 7, 2100142.
- [33] R. D. Nikam, J. Lee, W. Choi, D. Kim, H. Hwang, *ACS Nano* **2022**, 16, 12214.
- [34] A. Melianas, M.-A. Kang, A. VahidMohammadi, T. J. Quill, W. Tian, Y. Gogotsi, A. Salleo, M. M. Hamedi, *Adv. Funct. Mater.* **2022**, 32, 2109970.
- [35] Y. Li, T. P. Xiao, C. H. Bennett, E. Isele, A. Melianas, H. Tao, M. J. Marinella, A. Salleo, E. J. Fuller, A. A. Talin, *Front. Neurosci.* **2021**, 15, 636127.
- [36] M. T. Sharbati, Y. Du, J. Torres, N. D. Ardolino, M. Yun, F. Xiong, *Adv. Mater.* **2018**, 30, 1802353.
- [37] D. Kireev, S. Liu, H. Jin, T. P. Xiao, C. H. Bennett, D. Akinwande, J. A. C. Incorvia, *Nat. Commun.* **2022**, 13, 4386.
- [38] Y. Tuchman, T. J. Quill, G. LeCroy, A. Salleo, *Adv. Electron. Mater.* **2021**, 8, 2100426.
- [39] E. J. Fuller, Y. Li, C. Bennet, S. T. Keene, A. Melianas, S. Agarwal, M. J. Marinella, A. Salleo, A. A. Talin, *IBM J. Res. Dev.* **2019**, 63, 9:1.
- [40] S. T. Keene, A. Melianas, Y. van de Burgt, A. Salleo, *Adv. Electron. Mater.* **2019**, 5, 1800686.
- [41] Y. Li, J. Lu, D. Shang, Q. Liu, S. Wu, Z. Wu, X. Zhang, J. Yang, Z. Wang, H. Lv, M. Liu, *Adv. Mater.* **2020**, 32, 2003018.
- [42] Q. Wan, M. Rasetto, M. T. Sharbati, J. R. Erickson, S. R. Velagala, M. T. Reilly, Y. Li, R. Benosman, F. Xiong, *Adv. Intell. Syst.* **2021**, 3, 2100021.
- [43] M. Baldo, D. Ielmini, in *2021 IEEE International Memory Workshop (IMW)*, IEEE, Dresden, Germany **2021**, <https://doi.org/10.1109/IMW51353.2021.9439608>.
- [44] Y. Jeong, H. Lee, D. G. Ryu, S. H. Cho, G. Lee, S. Kim, S. Kim, Y. S. Lee, *Adv. Electron. Mater.* **2021**, 7, 2100185.
- [45] S. Kazemzadeh, L. Dodsworth, I. F. Pereira, Y. van de Burgt, *Adv. Electron. Mater.* **2022**, <https://doi.org/10.1002/aelm.202200427>.
- [46] A. A. Talin, Y. Li, D. A. Robinson, E. J. Fuller, S. Kumar, *Adv. Mater.* <https://doi.org/10.1002/adma.202204771>.
- [47] M. Onen, N. Emond, J. Li, B. Yildiz, J. A. del Alamo, *Nano Lett.* **2021**, 21, 6111.
- [48] A. Melianas, T. J. Quill, G. LeCroy, Y. Tuchman, H. v. Loo, S. T. Keene, A. Giovannitti, H. R. Lee, I. P. Maria, I. McCulloch, A. Salleo, *Sci. Adv.* **2020**, 6, eabb2958.
- [49] S. M. Haile, *Acta Mater.* **2003**, 51, 5981.
- [50] T. Gokmen, Y. Vlasov, *Front. Neurosci.* **2016**, 10, 333.
- [51] G. A. Niklasson, C. G. Granqvist, *J. Mater. Chem.* **2007**, 17, 127.
- [52] S. T. Keene, A. Melianas, E. J. Fuller, Y. van de Burgt, A. A. Talin, A. Salleo, *J. Phys. D: Appl. Phys.* **2018**, 51, 224002.
- [53] B. Traoré, P. Blaise, E. Vianello, H. Grampeix, S. Jeannot, L. Perniola, B. De Salvo, Y. Nishi, *IEEE Trans. Electron Devices* **2015**, 62, 4029.
- [54] Y. Y. Chen, R. Degraeve, S. Clima, B. Govoreanu, L. Goux, A. Fantini, G. S. Kar, G. Pourtois, G. Groeseneken, D. J. Wouters, M. Jurczak, in *2012 Int. Electron Devices Meeting*, IEEE, San Francisco, USA **2012**, pp. 20.3.1–20.3.4.
- [55] Z. Wei, T. Takagi, Y. Kanzawa, Y. Katoh, T. Ninomiya, K. Kawai, S. Muraoka, S. Mitani, K. Katayama, S. Fujii, R. Miyayama, Y. Kawashima, T. Mikawa, K. Shimakawa, K. Aono, presented at *2012 4th IEEE International Memory Workshop*, IEEE, Milan, Italy **2012**.
- [56] Y. Y. Chen, L. Goux, S. Clima, B. Govoreanu, R. Degraeve, G. S. Kar, A. Fantini, G. Groeseneken, D. J. Wouters, M. Jurczak, *IEEE Trans. Electron Devices* **2013**, 60, 1114.
- [57] C. M. Proctor, J. Rivnay, G. G. Malliaras, *J. Polym. Sci., Part B: Polym. Phys.* **2016**, 54, 1433.
- [58] M. Z. Bazant, *Acc. Chem. Res.* **2013**, 46, 1144.
- [59] H. Tian, M. Z. Bazant, *Nano Lett.* **2022**, 22, 5866.
- [60] Y. Li, W. C. Chueh, *Annu. Rev. Mater. Res.* **2018**, 48, 137.
- [61] Y. Li, H. Chen, K. Lim, H. D. Deng, J. Lim, D. Fraggedakis, P. M. Attia, S. C. Lee, N. Jin, J. Moškon, Z. Guan, W. E. Gent, J. Hong, Y.-S. Yu, M. Gaberšček, M. S. Islam, M. Z. Bazant, W. C. Chueh, *Nat. Mater.* **2018**, 17, 915.
- [62] J. Lim, Y. Li, D. H. Alsem, H. So, S. C. Lee, P. Bai, D. A. Cogswell, X. Liu, N. Jin, Y. Yu, N. J. Salmon, D. A. Shapiro, M. Z. Bazant, T. Tylliszczak, W. C. Chueh, *Science* **2016**, 353, 566.
- [63] C. S. Pedersen, J. H. Chang, Y. Li, N. Pryds, J. M. Garcia Lastra, *APL Mater.* **2020**, 8, 071108.
- [64] J. W. Cahn, J. E. Hilliard, *J. Chem. Phys.* **1958**, 28, 258.
- [65] B. König, O. J. J. Ronsin, J. Harting, *Phys. Chem. Chem. Phys.* **2021**, 23, 24823.
- [66] Q. Lu, B. Yildiz, *Nano Lett.* **2016**, 16, 1186.